Biosensors and Bioelectronics 244 (2024) 115777

Contents lists available at ScienceDirect

Biosensors and Bioelectronics

journal homepage: www.elsevier.com/locate/bios

Rapid estimation of electroporation-dependent tissue properties in canine lung tumors using a deep neural network

Edward J. Jacobs IV [a,b,*], Kenneth N. Aycock [a], Pedro P. Santos [a,c], Joanne L. Tuohy [d], Rafael V. Davalos [a,b]

[a] Department of Biomedical Engineering and Mechanics, Virginia Tech and Wake Forest University, Blacksburg, VA, USA
[b] Wallace H. Coulter Department of Biomedical Engineering, Georgia Tech and Emory University, Atlanta, GA, USA
[c] Department of Electrical Engineering, Federal University of Santa Catarina, Florianópolis, SC, Brazil
[d] Department of Small Animal Clinical Sciences, Virginia-Maryland College of Veterinary Medicine, Blacksburg, VA, USA

ARTICLE INFO

Keywords:
Electroporation
Electric tissue properties
Cancer
Deep neural network
Artificial intelligence
Finite element methods
Tissue ablation
Pulsed field ablation

ABSTRACT

The efficiency of electroporation treatments depends on the application of a critical electric field over the targeted tissue volume. Both the electric field and temperature distribution strongly depend on the tissue-specific electrical properties, which both differ between patients in healthy and malignant tissues and change in an electric field-dependent manner from the electroporation process itself. Therefore, tissue property estimations are paramount for treatment planning with electroporation therapies. *Ex vivo* methods to find electrical tissue properties often misrepresent the targeted tissue, especially when translating results to tumors. A voltage ramp is an *in situ* method that applies a series of increasing electric potentials across treatment electrodes and measures the resulting current. Here, we develop a robust deep neural network, trained on finite element model simulations, to directly predict tissue properties from a measured voltage ramp. There was minimal test error ($R^2 > 0.94$; $p < 0.0001$) in three important electric tissue properties. Further, our model was validated to correctly predict the complete dynamic conductivity curve in a previously characterized *ex vivo liver* model ($R^2 > 0.93$; $p < 0.0001$) within 100 s from probe insertion, showing great utility for a clinical application. Lastly, we characterize the first reported electrical tissue properties of lung tumors from five canine patients ($R^2 > 0.99$; $p < 0.0001$). We believe this platform can be incorporated prior to treatment to quickly ascertain patient-specific tissue properties required for electroporation treatment planning models or real-time treatment prediction algorithms. Further, this method can be used over traditional *ex vivo* methods for *in situ* tissue characterization with clinically relevant geometries.

1. Introduction

Electroporation is a biophysical phenomenon in which external pulsed electric fields (PEFs) generate nanoscale pores in the plasma membrane (Weaver and Chizmadzhev, 1996). The transitory formation of pores is called reversible electroporation (rEP) and has been used to successfully deliver chemotherapeutics (Mir et al., 1991; Sersa et al., 1998; Serša et al., 2000), genes (Neumann et al., 1982; Chu et al., 1987), and substances that would otherwise be impermeant into the cell. With the application of larger and longer potentials, the pores in the cellular membrane persist long enough, so the cells can no longer maintain homeostasis and die through various cell death mechanisms, such as necrosis or apoptosis (Aycock and Davalos, 2019). This is termed irreversible electroporation (IRE) and is used to generate clinically relevant ablation volumes without the need for adjuvant therapies and without significant thermal heating (Edd et al., 2006; Davalos et al., 2005; Al-Sakere et al., 2007). PEFs are being used clinically to treat atrial fibrillation (Sugrue et al., 2018) and skin (Serša et al., 2000), liver (Stillström et al., 2019; Kalra et al., 2019; Cheung et al., 2013), kidney (Benway, 2011), prostate (Guenther et al., 2019; Collettini et al., 2019), and pancreatic malignancies (Martin et al., 2013).

The mechanisms and efficiency of electroporation depend heavily on burst number, applied potential, and pulse duration (Weaver et al., 2012). A critical electric field magnitude is needed to encompass the desired tissue volume for treatment, thus prospective methods for modeling the electric field distribution within the tissue are often

* Corresponding author. 313 Ferst Dr NW, Atlanta, GA 30332, USA.
E-mail address: edwardj@gatech.edu (E.J. Jacobs).

https://doi.org/10.1016/j.bios.2023.115777
Received 23 May 2023; Received in revised form 8 October 2023; Accepted 20 October 2023
Available online 21 October 2023

required. The distribution of the electric field is strongly dependent on the electrical tissue properties, which vary significantly between patients in both healthy and malignant tissues (Beitel-White et al., 2021; Josowitz et al., 2014). Therefore, methods to accurately estimate tissue properties are needed for electroporation models, treatment planning, and treatment monitoring.

Conventional methods for tissue characterization use *ex vivo* tissue slices placed between flat plate electrodes to find the impedance at different applied electric field magnitudes. The tissue is often cut to a specified geometry, so the impedance can be related to tissue conductivity using a calculated shape factor. Quantifications are often limited to healthy animal tissues and can misrepresent the targeted tissue, especially when translating results to malignant tissues (Beitel-White et al., 2021; Hendricks-Wenger et al., 2021; Brock et al., 2020). Tissue characterization using patient derived xenografts is more representative, but they can take weeks to grow, are not widely available during treatment planning, and do not replicate *in situ* conditions (Aycock, 2022a; Brock et al., 2020). Further, even within a specific tumor type, there can be a high degree of tumor tissue heterogeneity between patients and even between tumors at different locations in the body. Translating experimentally found properties to an individual can be unreliable, so improved methods for patient specific tissue characterizations are greatly needed.

A voltage ramp (VR) is an *in situ* method that applies a series of increasing electric potentials (i.e. 25–2250 V) across the treatment electrodes to induce electric fields ranging from well below to above the electroporation threshold. The tissue impedance is a function of the applied potential, so both the applied voltage and resulting current are measured, and finite element modeling is employed to estimate the tissue properties. The electroporation-dependent tissue properties (bulk tissue conductivity, tissue conductivity due to electroporation effects, and fitting parameters) are iterated until the simulated current matches the measured current from the VR. This method was developed by our group and is being used for academic purposes, because a major limitation for its adoption and use in the clinic is the time it takes to gather the *in situ* VR data, then simulate the VR with a variety of tissue characteristics to match the currents. There are many models for use in treatment planning and monitoring during electroporation treatments (Perera-Bel et al., 2020, 2022; Marino et al., 2021; Campelo et al., 2022; Jacobs et al., 2023a), but they require *a priori* knowledge of the tissue

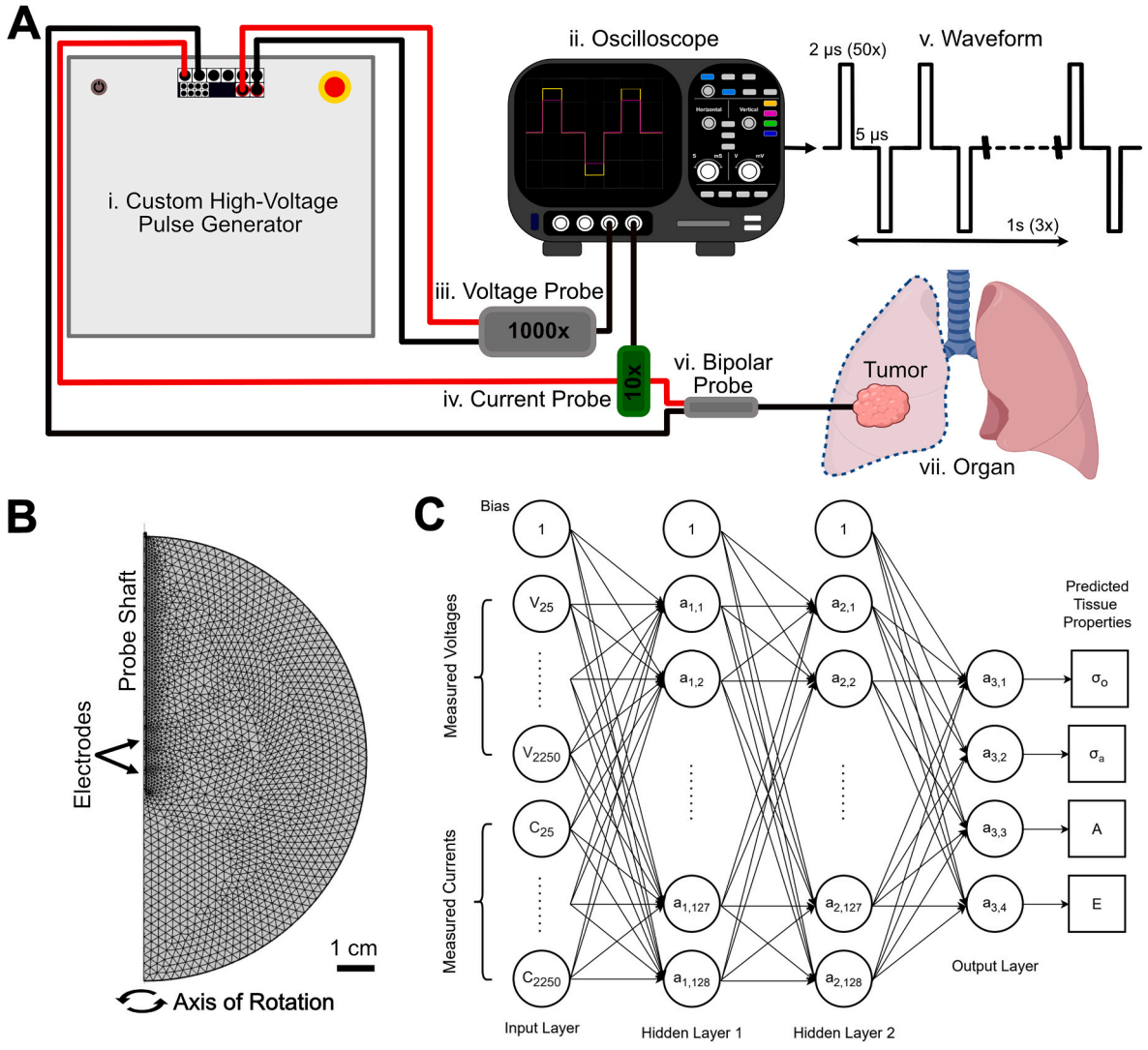

Fig. 1. A) Experimental Setup. The (i) Pulse generator was monitored using an (ii.) oscilloscope attached to a (iii.) 1000× attenuated high-voltage probe and (iv.) 10× attenuated current probe. (v.) A biphasic 2 µs pulse with 5 µs interpulse delay (repeated 50×). Each burst was applied at a 1s repetition rate. (vi.) A single insertion bipolar probe was used to deliver current directly into the (vii.) target organ or tissue. **B)** The probe insertion was replicated in COMSOL Multiphysics™ using a 2D axisymmetric geometry with an extra fine mesh size. **C)** The measured applied voltages and resulting currents from the voltage ramp were used as the input parameters to the deep neural network, with the tissue properties as the output parameters.

properties. The ability to rapidly estimate *in situ* tissue properties would then allow for more accurate intraoperative or intraprocedural models, thus improving electroporation treatments.

Here, we developed an accurate and robust deep neural network (DNN) to directly predict tissue properties from an *in situ* VR. We show that this model can be implemented prior to treatments to rapidly and accurately predict electroporation-dependent tissue properties. Lastly, we demonstrate that the DNN can predict the unique electrical tissue properties of five canine lung tumor patients from their *in situ* VRs. We believe our DNN can be incorporated prior to treatment to quickly ascertain tissue properties needed in other electroporation treatment planning models.

2. Materials and methods

2.1. Creating a numerical model for current simulations

To generate the dataset which the DNN was trained on, a two-dimensional axisymmetric finite element model (FEM) was employed in COMSOL™ Multiphysics 6.1 (COMSOL, Stockholm, Sweden) to simulate individual currents resulting from nine applied potential: 25, 50, 100, 250, 500, 1000, 1500, 2000, and 2250 V. The tissue was modeled as an ellipsoid of dimensions 10 cm x 5 cm x 5 cm with the axis of symmetry being the center axis of the probe shaft (Fig. 1B). A single insertion bipolar probe was modeled as two cylinders with radius, r_e, and length, l_e, constituting the source and sink electrodes. The two electrodes were separated by insulation with radius, r_e, and length, l_i. The electric potential, Φ, at the end of an IRE pulse was calculated with a modified Laplace equation under the electro-quasistatic approximation:

$$\nabla \bullet \left(\sigma\left(\left|\vec{E}\right|\right)\nabla\Phi\right) = 0 \tag{1}$$

where the electrical conductivity, σ, is a function of the local electric field magnitude $\left|\vec{E}\right|$ (Fig. 4C). The dynamic conductivity is solved in the steady state solution and can be calculated with:

$$\sigma\left(\left|\vec{E}\right|\right) = \sigma_o + \frac{\sigma_a}{1 - e^{-A\cdot\left(\left|\vec{E}\right| - E\right)}} \tag{2}$$

where σ_o is the baseline tissue conductivity, σ_a is the maximum change in conductivity due to electroporation within the tissue, and A and E are empirically determined sigmoidal fit parameters. E is the center point along the sigmoid transition, corresponding with the electric field threshold required to induce electroporation-dependent conductivity changes in tissue.

The boundary of the electrodes in contact with the tissue was set to $\Phi = V$ and $\Phi = 0$, for the source and sink, respectively. The outer boundary of the tissue was treated as electrically insulated. The resulting electric field was calculated as:

$$\vec{E} = -\nabla\Phi \tag{3}$$

2.2. Creating an input and output dataset for the deep neural network

We chose to use a regression DNN, trained with supervised learning. The input to the DNN would be the voltage and current data, read from a VR and the output would be the dynamic tissue properties. All the parameters within the sigmoid function were randomly chosen using independent uniform distributions to generate 50,000 unique sets of dynamic tissue properties. The chosen boundaries for the uniform distribution range the possible values for electrical tissue properties, and the distributions are given in Table 1. The nine applied electric potentials were chosen based off previously used VRs in the clinic. It is also the VR that was used here, prior to the treatments of five canine lung tumor patients. The VR electric potentials were previously arbitrarily chosen but are frequently used, so we kept these values and explored the individual impact they have in predicting tissue properties. The actual applied potentials can vary from the desired applied potentials set in the generator software. These variations have a direct impact on the applied current and, subsequently, the tissue property predictions. To account for potential deviations in applied potentials, we randomly chose potentials from normal distributions, with means at the desired value and standard deviations of 5% the desired values.

Table 1
Varied COMSOL parameters.

Parameters	Symbol	Value(s)
Probe Radius	r_e [mm]	0.8
Electrode Lengths	l_e [mm]	8
Insulation Length	l_i [mm]	7
Bulk Tissue Conductivity	σ_o [S·m^{-1}]	X ~ U[0.1, 0.6]
Increase in Electroporated Tissue Conductivity	σ_a [S·m^{-1}]	X ~ U[0.1, 0.6]
Fitting Parameter (Slope)	A [cm·V^{-1}]	X ~ U[0.002, 0.01]
Fitting Parameter (Midpoint)	E [V·cm^{-1}]	X ~ U[500, 1500]
Applied Voltages	V [V]	25 ~ J(25, 1.25), 50 ~ J(50, 2.5), 100 ~ J(100, 5), 250 ~ J(250, 12.5) 500 ~ J(500, 25), 1000 ~ J(1000, 50) 1500 ~ J(1500, 75), 2000 ~ J(2000, 100) 2250 ~ J(2250, 112.5)

U[min, max] uniform distribution; J(mean, std) Gaussian distribution.

Both the randomized tissue properties and electric potentials were imported into COMSOL™ Multiphysics to simulate the resulting current from the source electrode surface. The currents were matched to each applied potential, creating the input dataset, and the tissue properties made up the output dataset. 5% of the total dataset (2,500 samples) was set aside prior to training the DNN to form the test dataset. It should be noted that this is data that the DNN is not trained on.

2.3. Creating and training a deep neural network for electrical tissue property prediction

A simple two-layer DNN was defined and trained within Google Colab (Alphabet) using the Keras python interface for the TensorFlow library (Fig. 1C). There were 18 input features (9 voltages and 9 currents) and two hidden layers, each with 128 neurons and a rectified linear activation function (ReLu). The output layer had 4 neurons with a sigmoid activation function. The final DNN had 5,504 total trainable parameters. The model was trained with the mean squared error (MSE) loss function and Adam optimizer over 50 epochs. Validation during training was performed with 10-fold cross validation that was shuffled every epoch.

2.4. Voltage ramp and treatment for ex vivo liver validation

The DNN developed in this work was experimentally validated using an *ex vivo* porcine liver model. Porcine livers were excised at a local abattoir within 15 min of euthanasia and transported on ice. Experiments were performed at room temperature (23 °C, measured) within 90 min following organ excision to reduce the impact of degradation on the measured tissue impedance.

Electrical impedance spectroscopy (EIS), VR, and treatment were all performed at the same insertion location to mimic realistic treatment conditions. EIS was performed prior to the VR, after the VR, and after the treatment using a potentiostat (Reference 600, Gamry Instruments). Impedance and phase were measured from 1 Hz to 1 GHz (Supplemental Fig. S1). After the initial EIS measurement, a custom high-voltage generator (Voltmed Inc., Blacksburg, VA) was used to deliver a series of 3 bursts at each of the 9 voltages mentioned above at the same

location. Each burst was constructed of 2 μs biphasic pulses, each separated by a 5 μs delay, and repeated until 100 μs of energized time was achieved (Fig. 1). The dynamic conductivity curve varies for different applied pulse widths (Martin et al., 2013), so the VR must use the same applied pulsing scheme as the chosen treatment. The VR performed for the canine treatment plan (Method 2.5) was done with a 2 μs pulse width, so we used the same pulsing scheme for the *ex vivo* liver experiments.

During pulse delivery, the applied voltages and currents were monitored with a 1000× high-voltage attenuator (Enhancer 3000, Harvard Apparatus, Holliston, MA) and 10× attenuated passive current probe (Pearson Electronics, Palo Alto, CA) connected to a 4 GS/s oscilloscope (WaveSurfer 3024z, Teledyne LeCroy, Chestnut Ridge, NY). A custom python script was used to immediately extract the applied waveform saved to the oscilloscope (1.2 s for the entire VR). The time-series voltage and current data were processed and the last 250 ns of the last pulse within a given burst was averaged to obtain a singular voltage and current value for that burst. At each administered voltage, values extracted from each of the three bursts were averaged to build the input to the DNN. After the VR, the trained neural network then predicted the electric tissue properties (<0.1 s) and subsequent dynamic conductivity curve (eq (2)). The time from the start of the voltage ramp to obtaining the tissue-specific electrical properties was recorded using a timer.

Following the VR, without removing the probe, a treatment consisting of 100 bursts at 2250 V was delivered. Again, the voltage and current were recorded using the same methods mentioned above. The recorded voltage and current values obtained were compared to those simulated using the AI-predicted tissue values at the same location. A time-dependent COMSOL™ Multiphysics model was implemented to predict the electric field, temperature, and thermal damage distribution as previously described by our group (Aycock et al., 2022b; Beitel-White, 2021; Jacobs IV et al., 2023b).

2.5. Voltage ramp for canine patient lung tumors tissue characterization

The DNN developed in this work was used to estimate the tissue properties using VR data collected in five canine lung tumor patients treated with high-frequency IRE at the Virginia-Maryland College of Veterinary Medicine (Blacksburg, VA, USA). Once the bipolar electrode was inserted into the target tumor, but before treatment was started, a VR was administered. Briefly, a custom high-voltage generator (Voltmed Inc., Blacksburg, VA) was used to deliver a series of 3 bursts at each of the 9 voltages mentioned above (Fig. 1A). Each burst was constructed of 2 μs biphasic pulses, separated by 5 μs delays, and repeated until 100 μs of energized time was achieved. During pulse delivery, applied voltages and currents were monitored with a 1000× high-voltage attenuator (Enhancer 3000, Harvard Apparatus, Holliston, MA) and 10× attenuated passive current probe (Pearson Electronics, Palo Alto, CA) connected to an 4 GS/s oscilloscope (WaveSurfer 3024z, Teledyne LeCroy, Chestnut Ridge, NY). A custom script was written in MATLAB (Mathworks Inc., Natick, MA) in which the voltage and current during the last 250 ns of the last pulse within each burst were extracted and averaged. At each administered voltage, these three voltage and current datapoints were again averaged to build the dataset for each canine patient.

3. Results

3.1. The model accurately predicts electrical tissue properties from the simulation test dataset

The DNN was trained for 50 epochs to minimize the MSE loss function, and the model error quickly converged within 10 epochs and plateaued before the end of training. The validation dataset and training dataset did not diverge, suggesting the model was not overfit (Fig. 2A). The percent error (Fig. 2B) and the linear regression (Fig. 2C) were compared between the AI predicted and the COMSOL Multiphysics™ simulated electric tissue values from the test dataset. The bulk conductivity (σ_o), change in conductivity (σ_a), and midpoint (E) all had a low percent error. The quartiles for the percent error were all <1 %, and the R^2 values were >0.94. This suggests the trained model can translate the relationship found between the voltage and current readings and these tissue properties to data it has not explicitly seen before.

One of the tissue parameters, the slope fitting parameter (A), showed a uniform error and minimal correlation between the predicted and real parameter ($R^2 = 0.1477$). In the finite element model, we saw that while keeping the other parameters (σ_o, σ_a, E) constant at the median, varying A from 0.002 cm/V to 0.01 cm/V only led to an 10.4% difference in

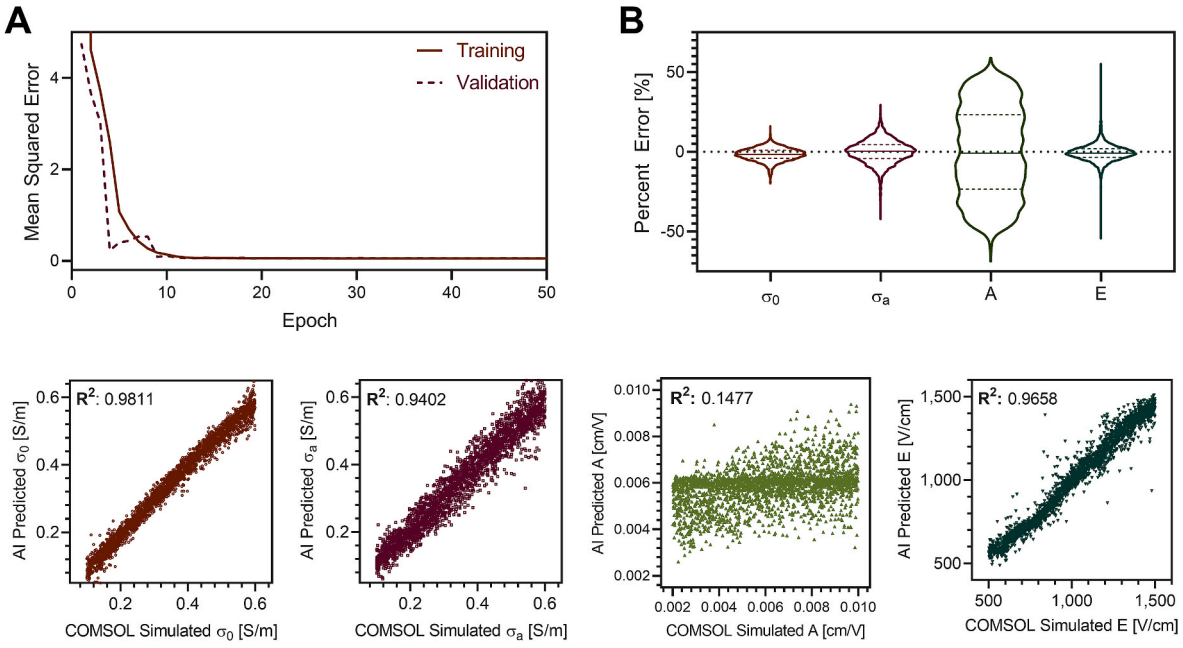

Fig. 2. The trained DNN has high accuracy in predicting fundamental electroporation-dependent tissue properties in the test dataset. A) Training and Validation Mean Squared Error over model training. **B)** Percent error and **C)** linear regression between the AI predicted parameters and the COMSOL parameters.

current. This is reflected further in simulated ablation volumes (800 V/cm lethal threshold for the 2 μs pulse width) only differing 1.6% over the A range. There may not be as strong a relationship between A and targets of electroporation modeling as the other parameters.

3.2. Each applied potential was influential in predicting certain tissue properties

We investigated the relationship between the voltages and currents within the VR and the tissue properties using the Shapley Additive exPlanations (SHAP) library within Python. SHAP operates through cooperative game theory to find the importance of an input feature on the output metric (Ribeiro et al., 2016; Štrumbelj and Kononenko, 2014). SHAP values were calculated and normalized for each input parameter to the DNN (Fig. 3). We represent the applied voltage, V_p, and resulting current, C_p, within each ramp by the intended applied potential, p (i.e. V_{50} and C_{50} are the recorded or simulated voltage and current when applying 50 V, respectively). The SHAP values show that current had more influence overall on the model error and prediction than voltage. The resulting currents (C_{25}, C_{50}, and C_{100}) from the lowest applied potentials had the most influence on the prediction of bulk conductivity (σ_o). Both the change in conductivity (σ_a) and midpoint fitting parameter (E) were influenced by currents throughout the entire VR. The change in conductivity sets the maximum conductivity within the tissue due to electroporation effects and had the most influence at C_{100}, C_{2000} and C_{2250}, with a lowest influence at C_{1000} and C_{1500}. The midpoint fitting parameter (E) had the most influence at C_{100}, C_{1000}, and C_{1500}. The slope fitting parameter (A) only had a large influence at C_{1500}. While certain resulting current values were not influential on specific parameters, every current measurement was influential for predicting at least one tissue parameter.

3.3. Model validation in an ex vivo liver

To validate our tissue prediction AI model, we chose to use an *ex vivo* porcine liver, since its electroporation properties have been characterized (Beitel-White et al., 2021). Previously, our group used biopsy punches to produce cylinders of tissue samples, which allowed for easy calculations of the conductivity from the measured impedance, using the chosen shape factor. Our experiments were performed at room temperature (23 °C) to match the previous experimental conditions. The three tested locations yielded slightly different current measurements for the given applied voltages (Fig. 4A), which was reflected in the differences in their impedance measurements (Fig. 4B). Since each sample location was electrically unique from the other locations, the DNN predicted slightly different dynamic conductivity curves (Fig. 4C). The predicted bulk conductivities (σ_0, 0.105, 0.113, and 0.108 S/m) were not significantly different than those calculated previously using flat plate electrodes (0.113 S/m) (Beitel-White et al., 2021). A *t*-test showed that our predicted bulk conductivity was not significantly different from those previously measured ($p > 0.9$). Further, the predicted bulk conductivities are close to those found on the IT'IS foundation database for liver tissue, 0.11 S/m (IT'IS Database). Our predicted electroporated conductivity (σ_f, 0.214, 0.224, 0.231 S/m) was marginally higher than that previously found (0.195 S/m) using flat plate electrodes (Beitel-White et al., 2021); however, a *t*-test again did not show a significant difference between our predicted electroporated conductivity and previously characterized values ($p > 0.8$). Further, our predicted midpoint fitting parameter (E, 1400, 1345, and 1424 V/cm) was lower than previously found, 1620 V/cm.

We also used a potentiostat (Gamry™) to perform electrical impedance spectroscopy (EIS) prior to the voltage ramp, after the voltage ramp, and after a treatment with 100 bursts, while maintaining the probe in the same position. We found that calculated pre-VR impedance using the potentiostat matched the calculated impedance from the VR at low voltages (Supplement S2).

To validate that the predicted dynamic conductivity curve correctly represents that *in situ* location, we applied 100 bursts at the target voltage (2250 V) at the same location immediately following the VR (<1 min). The current was measured for each burst. Further, the DNN-predicted dynamic conductivity curve was used to simulate the treatment in COMSOL™ Multiphysics. The simulated current using the DNN-predicted dynamic conductivity curve was compared to the recorded current at that location. Fig. 4D gives both the simulated and measured current over treatment. Due to minor changes in tissue properties even within the same tissue, both the simulated and measured current differed between each location. The simulated current using the DNN-predicted dynamic conductivity was statistically similar to the real recorded current. The three tested locations matched with R^2 values 0.9526, 0.9337, and 0.9469, all with p-values <0.0001.

3.4. The trained neural network can accurately predict the electrical tissue properties for in situ canine lung tumors

To further validate that our model can accurately estimate electric tissue properties *in situ*, we characterized the electrical properties of five canine lung tumor patients using VR data that was previously gathered by our group prior to IRE treatment. We demonstrate that the DNN can predict the unknown electric tissue properties in a clinical setting. To the best of our knowledge, this is also the first study characterizing the dynamic conductivity of lung tumors. The DNN-predicted tissue properties are given in Table 2, and the constructed dynamic conductivity curve for each patient is given in Fig. 5B.

The lung tumors all have much lower impedance values than that seen in healthy liver (Fig. 5A). Further, there was much more variability in the electric tissue properties between each tumor, compared to the low variability found in the healthy liver (Fig. 5B). Finally, the predicted bulk conductivity, σ_0, is higher for each tumor than healthy lung (0.115 S/m) (IT'IS Database).

Since lung tumor electroporation properties are unknown and since *in situ* tissue properties can vary greatly (especially between tumors), we could not compare the predicted tissue properties with known values.

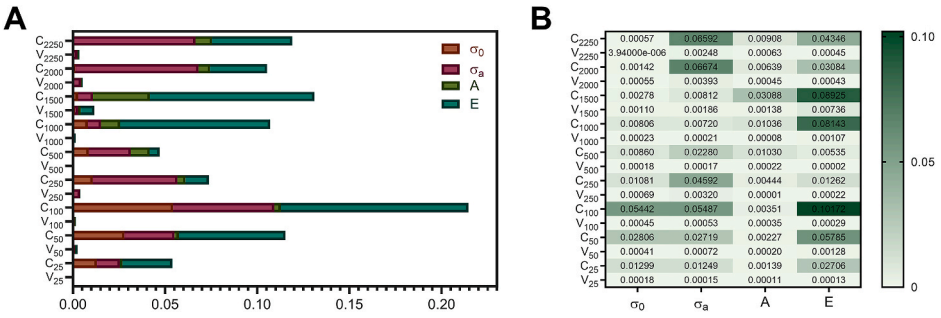

Fig. 3. Each voltage and current value within the voltage ramp was important in the overall model prediction. A) Normalized SHapley Additive exPlanations (SHAP) plot and **B**) heat map to explain the local influence model inputs have on the output.

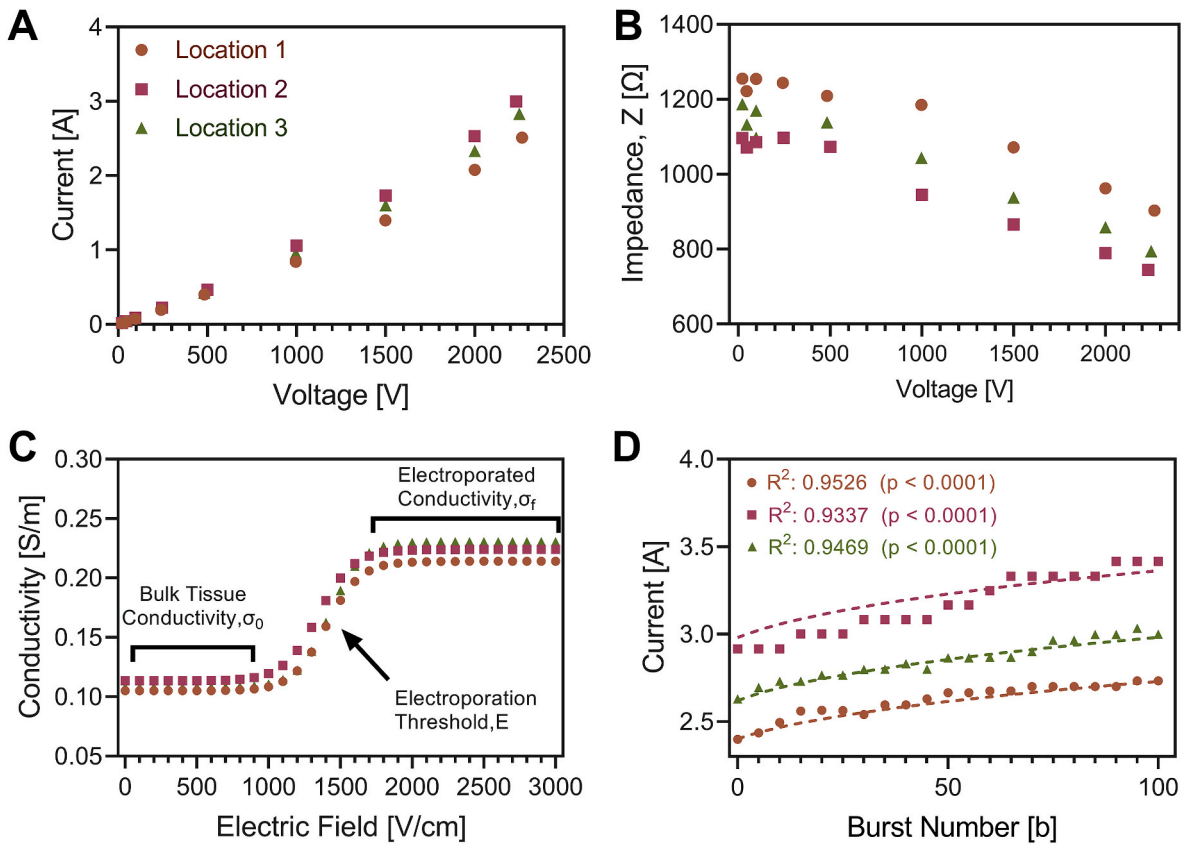

Fig. 4. The DNN-predicted dynamic conductivity correctly predicts the unique local tissue properties. A) Recorded voltage and current at 3 locations. **B)** Each location has a unique impedance in response to the applied electric field. **C)** The DNN predicted dynamic conductivity curves with similar values as previously characterized liver tissue. **D)** The simulated current (dashed) using the DNN-predicted dynamic conductivity curve and the recorded current (symbol) are not significantly different ($p < 0.0001$), with R^2 values of 0.9526, 0.9337, and 0.9469.

Table 2
Predicted canine lung tumor tissue properties.

	σ_0 [S/m]	σ_a [S/m]	σ_f [S/m]	A [cm/V]	E [V/cm]
Canine 1	0.234	0.346	0.58	0.00575	1022.6
Canine 2	0.233	0.233	0.466	0.00560	988.8
Canine 3	0.325	0.113	0.438	0.00558	950.4
Canine 4	0.316	0.589	0.905	0.00859	696.8
Canine 5	0.165	0.112	0.277	0.00859	999.4
Mean ±	0.255 ±	0.279 ±	0.529 ±	0.0068 ±	931.6 ±
STD	0.066	0.199	0.233	0.0016	133.8

Instead, the predicted values were defined for the tissue material properties within COMSOL™ Multiphysics, with the recorded voltages being the applied electrical potential. The simulated current was then compared with the known, recorded current from the *in situ* lung tumor VR. The simulated current matched the recorded current for each canine patient with R^2 values all above 0.9930 (Fig. 5C). The maximum error (Fig. 5D) and percent error (Fig. 5E) between the predicted and recorded currents was <2.8A and 25%, respectively. The mean and standard deviation indicate there is minimal error.

We were able to predict the unique electrical tissue properties for all five canine patients. To highlight the clinical need for obtaining prospective electrical properties, we simulated the electric field distribution, temperature distribution, and subsequent thermal damage for the five patients (Fig. 6). The dynamic conductivity curves for canines 1–3 did not vary greatly (Fig. 5B), so their simulations were similar. Canine 4 had a larger bulk conductivity, larger electroporated conductivity, and lower midpoint fitting parameter. The simulated electric field distribution is larger than the other patients, with the max simluated temperature rise >10 °C more than canines 1–3. The subsequent thermal damage volume was also 5× larger than for canines 1–3. Canine 5 was the opposite, with a lower bulk conductivity, a lower electroporated conductivity, and a higher midpoint fitting parameter. The estimated thermal heating was noticeably smaller with no indicated thermal damage.

4. Discussion

Currently, electroporation treatments are performed with mininal information about the tumors, with predictions about the electric field distribution done entirely *a priori*. Consequently, the electric field distributions could differ significantly from reality, with very few methods to validate or monitor treatment, often leading to under- or over-treatment. There is a trust that characterized tissue properties found in literature are representative of the target tissue, which leads to a risk if they vary significantly. The risk of heating and thermal damage can vary substantially between patients, organs, and even across tumors of the same type. Therefore, a "point-of-care" tool to measure patient-specific properties would allow for the most refined treatment predictions possible. In this study, we have demonstrated that an accurate and rapid electroporation-dependent tissue properties prediction model can be developed using finite element modeling of a VR. We saw the predictions converged to an accurate solution in three of the four tissue parameters and that the trained model can be translated for the tissue characterization of five canine lung tumor patients.

Our choice for applied potentials to use in our VR was based on previous tissue characterization and clinical work by our group (Neal et al., 2012; Partridge et al., 2020; O'Brien et al., 2019). The choice of voltages within the VR was arbitrary, so we characterized the

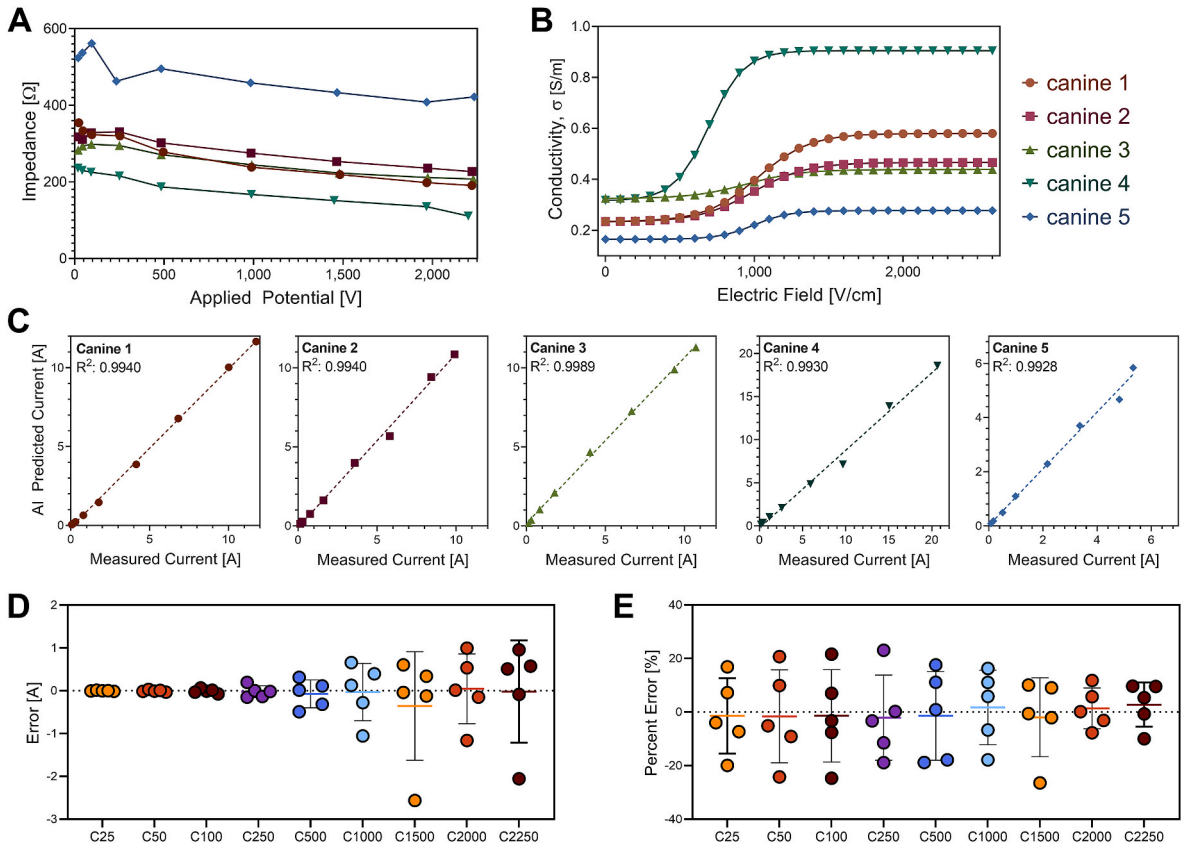

Fig. 5. The developed DNN can rapidly characterize *in situ* tissue properties in a clinical setting to obtain patient-specific tissue properties. A) Calculated impedance and **B)** predicted dynamic conductivity curves for the 5 canine lung tumors. **C)** Simulated current using the AI predicted tissue parameters versus the measured current. **D)** The relative and **E)** percent error between the simulated current using the AI predicted tissue parameters and the measured current.

contribution of each applied potential and resulting current in predicting electrical tissue properties for the first time. We saw that every applied electric potential was useful in the prediction of at least one property; however, any future changes to the VR should be checked using feature contribution analysis to minimize unnecessary energy delivered into the treatment tissue.

We found that the slope fitting parameter, A, was not as well predicted by a VR as the other tissue parameters. However, feature contribution analysis suggested that A does not have a large influence on the model output. Further, finite element modeling also showed a 10.4% difference in resulting current when varying A from its minimum value to maximum value; at its maximum the sigmoid acts like a Heaviside function and at its minimum it is almost a line (Martin et al., 2013). Within the tissue, there is a nonlinear electric field distribution with areas above and below the electric field threshold. At the lower applied potentials (25 V, 50 V, 100 V, and 250 V), there is very little or no tissue electroporation by the generated electric field, so these voltages had the most influence on predicting the bulk conductivity, σ_0. Similarly, at higher applied potentials (2000 V and 2250 V), there are larger amounts of tissue being electroporated, so these voltages had more influence on the electroporated conductivity, σ_a. The applied electric potentials which induce a progression in tissue conductivity changes are 500 V, 1000 V, and 1500 V; subsequently, these are the values that had the most influence on predicting the slope, A. These applied potentials may not contain enough information for the model to predict A, and adding additional readings at 1250 V and 1750 V might improve the resolution in this transition region. However, it seems unlikely since A does not influence current as significantly as the other parameters. This is further seen with the current simulations using the DNN-predicted liver dynamic conductivity curves; the simulated current and the recorded current were not significantly different. For this study, our dynamic conductivity curve incorporated the slope fitting parameter, A, to explore if our DNN could predict the value with reasonable accuracy. To our knowledge, no method has a validated A value, when compared to a known ground truth. A few models leave out A and assume a minimal transition range (Zhao et al., 2018), so future iterations of this model may remove A to decrease the trainable parameters.

The current limitation of our model is both the inflexibility to use voltages other than what the model is trained on and the rigid geometry chosen. We saw that C_{2000} and C_{2250} had the most influence on the change in conductivity, σ_a, but a larger applied potential may increase the accuracy where the dynamic conductivity curve has not plateaued. To insert additional voltages and currents into the input dataset, the finite element models would need to be run again with the new desired electric potentials, then matched to the exact tissue properties in the output dataset. The limit for how many potentials to add to the VR depends on the clinical safety of adding more or higher voltages, as well as the increased time needed to conduct the VR prior to beginning treatment. Voltages that generate an electric field above the lethal electric field threshold could partially treat the tissue, which may not be desired, but this effect should be minimal since the burst number is low (≤ 3) (Jacobs IV et al., 2023b). We confirmed this through the gathered EIS data prior to the VR, after the VR, and after treatment (Supplemental Fig. S1). We deliver three bursts within each ramp to minimize the unnecessary treatment of the tissue, but methods to gather electroporation specific properties must partially treat the tissue to characterize when this transition occurs.

We found that every applied voltage and resulting current was useful in the prediction, but to remove a specific ramp, we would simply remove the column corresponding to that voltage and current from the input dataset and retrain the DNN. The AI model itself is flexible to removing voltages, but it is not time efficient to add new voltages to the

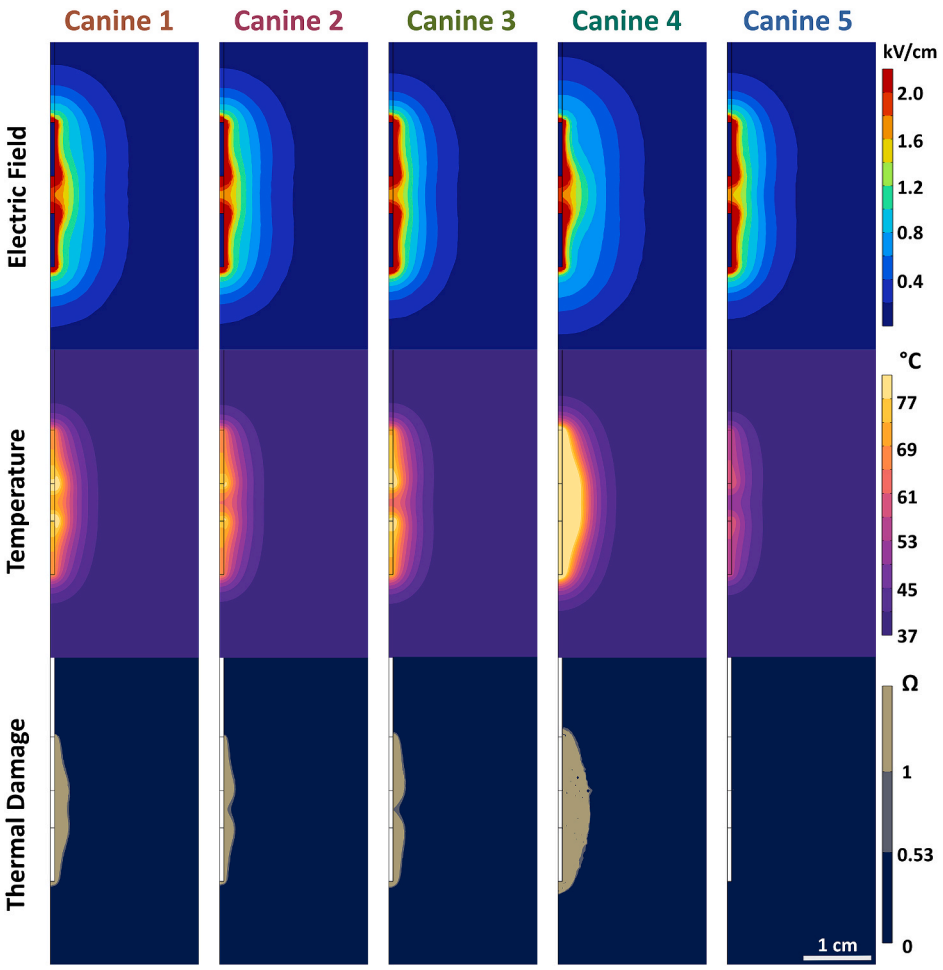

Fig. 6. 2D-axisymmetric FEM models of the electric field distribution, temperature distribution, and thermal damage volume highlight the clinical need for rapid patient-specific property predictions. Each tumor is electrically unique, which leads to varying electric field, temperature, and thermal distributions. (thermal damage: $\Omega > 0.53$).

dataset itself. Therefore, it may be beneficial to create a larger dataset with extra ramps (50V–3000V, step size 50V), so that dataset can be easily trimmed for a specific application. While temperature was not explicitly defined within our model, temperature-dependent conductivity changes are intrinsic to the tissue and will be reflected in the current read during the voltage ramp. Further, electroporation is a temperature-dependent process, and increases in temperature are shown to decreases the electroporation threshold (Aycock, 2022a; Fesmire et al., 2020). Therefore, to predict the dynamic conductivity at a specific temperature, the voltage ramp needs to be performed at that temperature. When characterizing tissue *in situ*, the voltage ramp and treatment are both performed at the same temperature.

While our DNN was trained using a dataset created with bipolar probe simulations, it can be trained on any number of datasets replicating any arbitrary geometry. DNNs trained using new geometries would need to be validated similarly to the one presented here. Decisions about what electrode geometry, voltages, and IRE waveform to use would need to be made before its use in the clinic, but, after the DNN is trained, it can be used repeatedly for that specific set up.

Electroporation treatments require accurate estimation of tissue properties for effective modeling and treatment planning. We saw that the DNN predicted unique electrical tissue values for each canine lung tumor. Since each tumor is electrically distinct from another, this should allow for personalization of each canine treatment versus using predefined properties found *ex vivo* or in other systems (Beitel-White, 2021; Brock et al., 2020; Hendricks-Wenger, 2021). Further, there are not already available electroporation tissue properties for most tumors. Since this model is easy to implement, we expect it to assist with characterizing the electroporation-dependent tissue properties of various tumors and tissues. However, *in situ* tissue properties should still be gathered prior to treatment, due to tumor heterogeneity. We saw large variations in measured current across all 5 canine patients (Fig. 5A), even though we applied the same electric potentials with the same probe geometry. Canine computed topography (CT) scans indicated that canine patient 4 had increased areas of hypoattenuation compared to the other patients (Supplemental Fig. S2). These areas can indicate necrotic tissue or fluid within the tumors, which can have higher conductivities than normal tissue (0.688–1.41 S/m) (IT'IS Database). Previous groups have tried to relate impedance changes with electroporation outcomes (Dunki-Jacobs et al., 2014), but the nonlinear nature of the electric field distribution makes it difficult to quantify the electric tissue properties. VRs can give detailed *in situ* information about a patient's tumor which opens avenues for correlating to patient outcomes and clustering groups for immunological or histopathological analysis.

Though VRs allow for more personalization, the method to extract tissue properties using finite element modeling is time consuming, greatly limiting its clinical application. We overcome this limitation with our time-efficient AI model, and we believe our model can be incorporated prior to treatment to quickly ascertain tissue properties needed in other electroporation treatment models. Of course, advances in treatment planning software will be necessary to realize this goal, but

significant progress has been made in recent years to rapidly predict the electric field and temperature distribution resulting from the applied treatment (Perera-Bel et al., 2020, 2022; Marino et al., 2021; Campelo et al., 2022; Jacobs et al., 2023a).

5. Conclusion

Here, we developed an accurate and robust deep neural network to rapidly and accurately predict electroporation-dependent electrical tissue properties. Through feature contribution calculations, we found each chosen voltage within the voltage ramp was important in the electrical tissue property prediction. There was minimal test error ($R^2 > 0.94$; $p < 0.0001$) in three important tissue properties (bulk conductivity, electroporation threshold, and conductivity change due to electroporation), with a uniform error in the slope fitting parameter. Our model was able to correctly predict the dynamic conductivity curve in a previously characterized *ex vivo* porcine liver model ($R^2 > 0.93$; $p < 0.0001$) within 100 s from probe insertion, showing great utility for a clinical application. Lastly, we characterized the first reported electrical tissue properties of lung tumors from five canine patients ($R^2 > 0.99$; $p < 0.0001$). We believe this platform can be incorporated prior to treatment to quickly ascertain electroporation-dependent electrical tissue properties critical for treatment planning models or real-time treatment prediction algorithms. Further, this method can be used over traditional *ex vivo* methods for *in situ* or patient-specific tissue characterization with clinically relevant geometries.

Acknowledgments and funding

This research was funded in part by the NIH R01 (R01CA24047) and the Veterinary Memorial Fund. We would like to acknowledge the Surgical Oncology clinical team at the Virginia-Maryland College of Veterinary Medicine for their assistance in gathering the voltage and current data during their treatment of canine lung tumor patients.

CRediT authorship contribution statement

Edward J. Jacobs: Conceptualization, Data curation, Formal analysis, Software, Investigation, Methodology, Validation, Visualization, Writing – original draft. **Kenneth N. Aycock:** Data curation, Investigation, Writing – review & editing. **Pedro P. Santos:** Data curation, Software, Investigation, Validation, Writing – review & editing. **Joanne L. Tuohy:** Investigation, Resources, Writing – review & editing. **Rafael V. Davalos:** Conceptualization, Supervision, Funding acquisition, Project administration, Writing – review & editing.

Declaration of competing interest

The authors declare the following financial interests/personal relationships which may be considered as potential competing interests: The authors have patents related to the paper. R.V.D. has ownership interest in startup companies within the field of bioelectrics. In addition, R.V.D. also receives royalty income from technologies he has invented and serves as a consultant.

Data availability

Data will be made available on request.

Appendix A. Supplementary data

Supplementary data to this article can be found online at https://doi.org/10.1016/j.bios.2023.115777.

References

Al-Sakere, B., et al., 2007. Tumor ablation with irreversible electroporation. Nov. PLoS One 2 (11) https://doi.org/10.1371/JOURNAL.PONE.0001135.

Aycock, K.N., Davalos, R.V., 2019. Irreversible electroporation: background, theory, and review of recent developments in clinical Oncology. Dec. Bioelectricity 1 (4), 214–234. https://doi.org/10.1089/BIOE.2019.0029/ASSET/IMAGES/LARGE/BIOE.2019.0029_FIGURE7.JPEG.

Aycock, K.N., et al., 2022a. Experimental and numerical investigation of parameters affecting high-frequency irreversible electroporation for prostate cancer ablation. J. Biomech. Eng. 144 (6) https://doi.org/10.1115/1.4053595.

Aycock, K.N., Campelo, S.N., Davalos, R.V., 2022b. A comparative modeling study of thermal mitigation strategies in irreversible electroporation treatments, 2022b J. Heat Tran. 144 (3). https://doi.org/10.1115/1.4053199.

Beitel-White, N., et al., 2021. Multi-tissue analysis on the impact of electroporation on electrical and thermal properties. Mar. IEEE Trans. Biomed. Eng. 68 (3), 771–782. https://doi.org/10.1109/TBME.2020.3013572.

Benway, B.M., 2011. Irreversible electroporation of renal cell carcinoma: a first-in-man phase I clinical study. Jan. Year Bk. Urol. 2011, 36–37. https://doi.org/10.1016/j.yuro.2011.06.061.

Brock, R.M., et al., 2020. Patient derived xenografts expand human primary pancreatic tumor tissue availability for ex vivo irreversible electroporation testing. Front. Oncol. 10, 843. https://doi.org/10.3389/FONC.2020.00843/BIBTEX.

Campelo, S.N., Jacobs, E.J., Aycock, K.N., Davalos, R.v., 2022. Real-time temperature rise estimation during irreversible electroporation treatment through state-space modeling. Sep. Bioengineering 9 (10), 499. https://doi.org/10.3390/BIOENGINEERING9100499, 2022, Vol. 9, Page 499.

Cheung, W., Kavnoudias, H., Roberts, S., Szkandera, B., Kemp, W., Thomson, K.R., 2013. Irreversible electroporation for unresectable hepatocellular carcinoma: initial experience and review of safety and outcomes. Technol. Cancer Res. Treat. 12 (3), 233–241. https://doi.org/10.7785/tcrt.2012.500317.

Chu, G., Hayakawa, H., Berg, P., 1987. Electroporation for the efficient transfecdon of mammalian cells with DNA. Nucleic Acids Res. 15. Dec. 06, 2022. [Online]. Available: https://academic.oup.com/nar/article/15/3/1311/1166855.

Collettini, F., et al., 2019. Image-guided irreversible electroporation of localized prostate cancer: functional and oncologic outcomes. Radiology 292 (1), 250–257. https://doi.org/10.1148/radiol.2019181987.

Dunki-Jacobs, E.M., Philips, P., Martin, R.C.G., 2014. Evaluation of resistance as a measure of successful tumor ablation during irreversible electroporation of the pancreas. Feb J. Am. Coll. Surg. 218 (2), 179–187. https://doi.org/10.1016/j.jamcollsurg.2013.10.013.

Edd, J.F., Horowitz, L., Davalos, R.v., Mir, L.M., Rubinsky, B., 2006. In vivo results of a new focal tissue ablation technique: irreversible electroporation. Jul. IEEE Trans. Biomed. Eng. 53 (7), 1409–1415. https://doi.org/10.1109/TBME.2006.873745.

Fesmire, C.C., Petrella, R.A., Kaufman, J.D., Topasna, N., Sano, M.B., 2020. Irreversible electroporation is a thermally mediated ablation modality for pulses on the order of one microsecond. Oct. Bioelectrochemistry 135, 107544 https://doi.org/10.1016/j.bioelechem.2020.107544.

Guenther, E., et al., 2019. Prostate cancer treatment with Irreversible Electroporation (IRE): safety, efficacy and clinical experience in 471 treatments. Apr. PLoS One 14 (4) https://doi.org/10.1371/journal.pone.0215093.

Hendricks-Wenger, A., et al., 2021. Establishing an immunocompromised porcine model of human cancer for novel therapy development with pancreatic adenocarcinoma and irreversible electroporation. Apr. Sci. Rep. 11 (1), 1–14. https://doi.org/10.1038/s41598-021-87228-5, 2021 11:1.

Jacobs, E., Campelo, S., Aycock, K., Yao, D., Davalos, R.V., 2023a. Spatiotemporal estimations of temperature rise during electroporation treatments using a deep neural network. Comput. Biol. Med., 107019 https://doi.org/10.1016/j.compbiomed.2023.107019.

Jacobs IV, E.J., Campelo, S., Charlton, A., Altreuter, S., Davalos, R.V., 2023b. Characterizing Reversible, Irreversible, and Calcium Electroporation to Generate a Burst-dependent Dynamic Conductivity Curve. Bioelectrochemistry, 108580. https://doi.org/10.1016/j.bioelechem.2023.108580.

Josowitz, A.D., et al., 2014. Predicting the electric field distribution in the brain for the treatment of glioblastoma. Phys. Med. Biol. 59, 4137. https://doi.org/10.1088/0031-9155/59/15/4137.

Kalra, N., et al., 2019. Irreversible electroporation for unresectable hepatocellular carcinoma: initial experience. Cardiovasc. Intervent. Radiol. 42 https://doi.org/10.1007/s00270-019-02164-2.

Marino, M., Luján, E., Mocskos, E., Marshall, G., 2021. OpenEP: an open-source simulator for electroporation-based tumor treatments. Dec. Sci. Rep. 11 (1) https://doi.org/10.1038/s41598-020-79858-y.

Martin II, R., Mcfarland, K., Ellis, S., Velanovich, V., 2013. Irreversible electroporation in locally advanced pancreatic cancer: potential improved overall survival. Ann. Surg Oncol. 20 https://doi.org/10.1245/s10434-012-2736-1.

Mir, L.M., Orlowski, S., Belehradek, J., Paoletti, C., 1991. Electrochemotherapy Potentiation of Antitumour Effect of Bleomycin by Local Electric Pulses.

Neal II, R.E., Garcia, P.A., Robertson, J.L., V Davalos, R., 2012. Experimental characterization and numerical modeling of tissue electrical conductivity during pulsed electric fields for irreversible electroporation treatment planning. IEEE Trans. Biomed. Eng. 59 (4) https://doi.org/10.1109/TBME.2012.2182994.

Neumann, E., Schaefer-Ridder, M., Wang, Y., Hofschneider, P.H., 1982. Gene transfer into mouse lyoma cells by electroporation in high electric fields. EMBO J. 1 (7), 841–845. https://doi.org/10.1002/j.1460-2075.1982.tb01257.x.

O'Brien, T.J., et al., 2019. Experimental high-frequency irreversible electroporation using a single-needle delivery approach for nonthermal pancreatic ablation in vivo.

J. Vasc. Intervent. Radiol. 30 (6), 854–862. https://doi.org/10.1016/J.JVIR.2019.01.032 e7, Jun.

Partridge, B.R., et al., 2020. High-frequency irreversible electroporation for treatment of primary liver cancer: a proof-of-principle study in canine hepatocellular carcinoma. Mar. J. Vasc. Intervent. Radiol. 31 (3), 482–491.e4. https://doi.org/10.1016/J.JVIR.2019.10.015.

Perera-Bel, E., et al., 2020. EView: an electric field visualization web platform for electroporation-based therapies. Comput. Methods Progr. Biomed. 197 [Online]. Available: www.visifield.com.

Perera-Bel, Enric, et al., 2022. Piret —a platform for treatment planning in electroporation-based therapies. IEEE 15, 449–470. https://doi.org/10.13039/501100011033.

Ribeiro, M.T., Singh, S., Guestrin, C., 2016. Why should I trust you?': explaining the predictions of any classifier. Feb. In: NAACL-HLT 2016 - 2016 Conference of the North American Chapter of the Association for Computational Linguistics: Human Language Technologies, Proceedings of the Demonstrations Session, pp. 97–101. https://doi.org/10.48550/arxiv.1602.04938.

Sersa, G., Stabuc, B., Cemazar, M., Jancar, B., Miklavcic, D., Rudolf, Z., 1998. Electrochemotherapy with Cisplatin: Potentiation of Local Cisplatin Antitumour Effectiveness by Application of Electric Pulses in Cancer Patients.

Serša, G., Stabuc, B., Miklavcic, D., Rudolf, Z., 2000. Electrochemotherapy with cisplatin: clinical experience in malignant melanoma patients. Clin. Cancer Res. 6, 863–867 [Online]. Available: http://aacrjournals.org/clincancerres/article-pdf/6/3/863/2076012/df030000863.pdf.

Stillström, D., Beermann, M., Engstrand, J., Freedman, J., Nilsson, H., 2019. Initial experience with irreversible electroporation of liver tumours. Jan. Eur. J. Radiol. Open 6, 62–67. https://doi.org/10.1016/J.EJRO.2019.01.004.

Štrumbelj, E., Kononenko, I., 2014. Explaining prediction models and individual predictions with feature contributions. Nov. Knowl. Inf. Syst. 41 (3), 647–665. https://doi.org/10.1007/s10115-013-0679-x.

Sugrue, A., et al., 2018. Irreversible electroporation for the treatment of cardiac arrhythmias. May 04, Expet Rev. Cardiovasc. Ther. 16 (5), 349–360. https://doi.org/10.1080/14779072.2018.1459185. Taylor and Francis Ltd.

Davalos, R.V., Mir, L.M., Rubinsky, B., 2005. Tissue ablation with irreversible electroporation. Ann. Biomed. Eng. 33 (2), 223–231. https://doi.org/10.1007/s10439-005-8981-8.

Weaver, J.C., Chizmadzhev, Y.A., 1996. Theory of Electroporation: A Review. Bioelectrochemistry and Bioenergetics 41 (2), 135–160.

Weaver, J.C., Smith, K.C., Esser, A.T., Son, R.S., Gowrishankar, T.R., 2012. A brief overview of electroporation pulse strength-duration space: a region where additional intracellular effects are expected. Oct. Bioelectrochemistry 87, 236–243. https://doi.org/10.1016/j.bioelechem.2012.02.007.

Zhao, Y., et al., 2018. Characterization of conductivity changes during high-frequency irreversible electroporation for treatment planning. IEEE Trans. Biomed. Eng. 65 (8) https://doi.org/10.1109/TBME.2017.2778101.

"IT'IS Database for thermal and electromagnetic parameters of biological tissues, Version 4.0. Available online: https://itis.swiss/virtual-population/tissue-properties/downloads/database-v4-1/(accessed on 15 August 2022)..".